

Low-Complexity Reconfigurable MIMO for Millimeter Wave Communications

Biao He, *Member, IEEE*, and Hamid Jafarkhani, *Fellow, IEEE*

Abstract—The performance of millimeter wave (mmWave) multiple-input multiple-output (MIMO) systems is limited by the sparse nature of propagation channels and the restricted number of radio frequency chains at transceivers. The introduction of reconfigurable antennas offers an additional degree of freedom on designing mmWave MIMO systems. This paper provides a theoretical framework for studying the mmWave MIMO with reconfigurable antennas. Based on the virtual channel model, we present an architecture of reconfigurable mmWave MIMO with beamspace hybrid analog-digital beamformers and reconfigurable antennas at both the transmitter and the receiver. We show that employing reconfigurable antennas can provide throughput gain for the mmWave MIMO. We derive the expression for the average throughput gain of using reconfigurable antennas in the system, and further derive the expression for the outage throughput gain for the scenarios where the channels are (quasi) static. Moreover, we propose a low-complexity algorithm for reconfiguration state selection and beam selection. Our numerical results verify the derived expressions for the throughput gains and demonstrate the near-optimal throughput performance of the proposed low-complexity algorithm.

Index Terms—Reconfigurable antennas, millimeter wave, sparse channels, virtual channel model, throughput gain.

I. INTRODUCTION

The fast development of wireless technology has enabled the ubiquitous use of wireless devices in modern life. Consequently, a capacity crisis in wireless communications is being created. A promising solution to the capacity crisis is to increase the available spectrum for commercial wireless networks by exploring the millimeter wave (mmWave) band from 30 GHz to 300 GHz.

MmWave communications has drawn significant attention in recent years [2], as the large available bandwidth may offer multiple-Gbps data rates [3]. In particular, the 3rd Generation Partnership Project (3GPP), which is a work in progress to serve as the international industry standard for 5G, has continuously published the technical report (TR) documents on the mmWave channels, e.g., [4–6]. Different from low-frequency communications, mmWave carrier frequencies are relatively very high. The high frequency results in some propagation challenges, such as large pathloss and severe shadowing [2]. Meanwhile, the small wavelength enables a large number of antennas to be closely packed to form mmWave large multi-antenna systems, which can be utilized to overcome the propagation challenges and provide reasonable signal to noise ratios (SNRs) [7]. The multi-input multi-output (MIMO)

technology has already been standardized and widely adopted in commercial WLAN and cellular systems at sub-6 GHz frequencies (IEEE 802.11n/ac, IEEE 802.16e/m, 3GPP cellular LTE, and LTE Advanced) [8, 9]. However, the performance of mmWave MIMO systems is still considerably limited due to the sparsity of the channels and the stringent constraint of using radio frequency (RF) chains in mmWave transceivers. The directional propagations and clustered scattering make the mmWave paths to be highly sparse [3]. More importantly, the high cost and power consumption of RF components and data converters preclude the adoption of fully digital processing for mmWave MIMO to achieve large beamforming gains [3, 10], and low-complexity transceivers relying heavily on analog or hybrid (analog-digital) processing are often adopted [11–13].

The limited beamforming capability and performance of mmWave MIMO motivate us to investigate the potential benefits of employing reconfigurable antennas for mmWave MIMO in this work. Different from conventional antennas with fixed radiation characteristics, reconfigurable antennas can dynamically change their radiation patterns, polarizations, and/or frequencies [14, 15], and offer an additional degree of freedom for designing mmWave MIMO systems. The radiation characteristics of an antenna is directly determined by the distribution of its current [16], and the mechanism of reconfigurable antennas is to change the current flow in the antenna, so that the radiation pattern, polarization, and/or frequency can be modified. The detailed relationship between the geometry of an antenna's current and how it radiates or collects the energy can be found in Equation (1) in [15]. The study of reconfigurable antennas for traditional low-frequency MIMO has received considerable attention, e.g., presented in [14, 15, 17–20]. From the practical antenna design perspective, different approaches to make antennas reconfigurable have been proposed and realized, such as Microelectrophoretical Systems (MEMS) switches, diodes, field-effect transistors (FETs), varactors, and optical switches [18–20]. From the perspective of theoretical performance analysis, the array gain, diversity gain, and coding gain [21] of employing reconfigurable antennas have been derived with space-time code designs [15, 17]. More recently, reconfigurable antennas for communications at mmWave frequencies have been designed and realized, e.g., [22] at 20.7–36 GHz, [23] at 92.6–99.3 GHz, and [24] at 28–38 GHz. The design of space-time codes for a 2×2 mmWave MIMO with reconfigurable transmit antennas was investigated in [25] and [26], and the achieved diversity gain and coding gain were demonstrated. Due to the simple structure of a 2×2 MIMO, neither the important sparse nature of mmWave channels nor the transceivers with low-complexity beamforming were considered in [25] and [26].

This work was presented in part at the 2018 IEEE International Conference on Communications (ICC) [1].

This work was supported in part by the NSF Award ECCS-1642536.

The authors are with the Center for Pervasive Communications and Computing, University of California at Irvine, Irvine, CA 92697, USA (email: {biao.he, hamidj}@uci.edu).

In this work, we comprehensively study the mmWave MIMO systems with reconfigurable antennas. We consider that the radiation patterns and/or the polarizations of antennas are reconfigurable, while do not consider the frequency reconfigurations. We consider general mmWave systems over sparse channels and the transceivers with low-complexity beamforming are taken into account. Our analytical results are generally applicable for the whole mmWave frequency range where the channel matrices are sparse provided the models are reflective of real systems. We present a practical architecture of mmWave MIMO with beamspace hybrid beamformers and reconfigurable antennas. The presented architecture has a low-complexity structure for practical implementation, since it only requires a few RF chains. More importantly, as will be shown later in the paper, the presented architecture offers tractable analytical results on the throughput gains of employing reconfigurable antennas. The throughput gains of employing reconfigurable antennas for the mmWave system are investigated, and a fast selection algorithm for the antennas' reconfiguration state and the hybrid beamformers' beams is further proposed.

The primary contributions of the paper are summarized as follows:

- 1) We are the first to provide a theoretical framework for studying the reconfigurable antennas in mmWave MIMO systems. We take the sparse nature of mmWave channels into account, and present a practical architecture of the mmWave MIMO with low-complexity beamformers and reconfigurable antennas, in which beamspace hybrid beamformers and reconfigurable antennas are employed at both the transmitter and the receiver.
- 2) We investigate the throughput gains of employing reconfigurable antennas in mmWave MIMO systems. We derive the expression for the average throughput gain, which involves an infinite integral of the error function. We further consider the cases of small and large numbers of reconfiguration states, and derive the corresponding simplified expressions for the average throughput gains. We also derive the expression for the outage throughput gain of employing reconfigurable antennas for the (quasi) static channels. Moreover, we analyze the limiting growth rates of the average throughput gain and the outage throughput gain as the number of reconfiguration states becomes large. To the best of our knowledge, the throughput gains of employing reconfigurable antennas have never been derived in the literature, even in the case of low-frequency systems.
- 3) With the highly sparse nature of the channel, the number of non-vanishing rows and columns of the channel matrix in beamspace domain is relatively small, and the dominant beams usually significantly outperform the others. Taking those advantages of the sparse nature of mmWave channels, we propose a fast algorithm for selecting the reconfiguration state of the antennas and the beams for the beamspace hybrid beamformers. The proposed algorithm significantly reduces the complexity of the reconfiguration state selection and beam selection without a large throughput loss compared with the optimal selection of

Table 1: Summary of notations.

symbol	meaning
\mathbf{X}^T	transpose of \mathbf{X}
\mathbf{X}^H	conjugate transpose of \mathbf{X}
$\mathbf{X}(m, n)$	entry of \mathbf{X} in m -th row and n -th column
$\text{Tr}(\mathbf{X})$	trace of \mathbf{X}
$ \mathbf{X} $	determinant of \mathbf{X}
$\ \mathbf{X}\ _F$	Frobenius norm of \mathbf{X}
$\text{Re}[x]$	real part of x
$\text{Im}[x]$	imaginary part of x
\odot	Hadamard (element-wise) product
$ \mathcal{X} $	cardinality of set \mathcal{X}
$\text{sgn}(\cdot)$	sign function
$\text{erf}(\cdot)$	error function
$\text{erf}^{-1}(\cdot)$	inverse error function
$\mathbb{E}\{\cdot\}$	expectation operation
$\mathbb{P}(\cdot)$	probability measure
$\text{corr}(\cdot, \cdot)$	correlation coefficient
\mathbf{I}_n	identity matrix of size n
$\mathcal{N}(\mu, \sigma^2)$	Gaussian distribution with mean μ and variance σ^2
$\mathcal{CN}(\mu, \sigma^2)$	complex Gaussian distribution with mean μ and variance σ^2
$\mathcal{CN}(\mathbf{a}, \mathbf{A})$	distribution of a circularly symmetric complex Gaussian random vector with mean \mathbf{a} and covariance matrix \mathbf{A}

- reconfiguration state and beams by exhaustive search.
- 4) We demonstrate the throughput gains of employing reconfigurable antennas in mmWave MIMO systems by numerical evaluations. A practical clustered multipath model is adopted for generating MIMO channels [27]. Our results show that the employment of reconfigurable antennas provides both the average throughput gain and the outage throughput gain for mmWave MIMO systems, and confirm the accuracy of our derived expressions. For the outage throughput, an interesting finding is that the performance gain increases as the required outage level becomes more stringent.

The notations are summarized in Table 1.

II. PRELIMINARIES

Different from conventional antennas with fixed radiation characteristics, reconfigurable antennas can dynamically change their radiation characteristics. The mechanism of reconfigurable antennas is to change the current flow in the antenna, so that the radiation pattern, polarization, and/or frequency can be modified. Specifically, the manner how an antenna radiates or captures the energy can be mathematically expressed as [15, 16]

$$\mathbf{F}(\theta, \phi) = \hat{\mathbf{r}} \times \left[\hat{\mathbf{r}} \times \left[\int_{V'} \mathbf{J}_{V'(\mathbf{r}')} e^{-j\beta \hat{\mathbf{r}} \mathbf{r}'} dV' \right] \right], \quad (1)$$

where $\mathbf{F}(\theta, \phi) = (F_\theta(\theta, \phi), F_\phi(\theta, \phi))^\dagger$ denotes the normalized complex amplitude radiation pattern of the antenna, $\mathbf{J}_{V'(\mathbf{r}')}$ denotes the current distribution in the antenna, \mathbf{r}' denotes the vector from the coordinate system's origin to any point on the antenna, $\hat{\mathbf{r}}$ denotes the unit vector in the direction of propagation (from the origin to the observation point), β denotes the propagation constant, V' denotes the volume of the antenna containing the volumetric current densities, and θ and ϕ denote the elevation and azimuth angles in the

spherical coordinate system, respectively. It is evident from (1) that one can change the current distribution $\mathbf{J}_{V'}(\mathbf{r}')$ by altering the antenna's physical configuration \mathbf{r}' , and finally modify the antenna's radiation characteristics $\mathbf{F}(\theta, \phi)$. There are different approaches to change the antenna's physical configuration in practice, e.g., microelectrophoretical systems (MEMS), diodes, field-effect transistors (FETs), varactors, and optical switches [18–20]. One can find examples of how the change in current distribution affects the antenna's radiation pattern, polarization, and frequency in [14]. The design of reconfigurable antennas for mmWave frequencies has been specifically investigated in, e.g., [22–24]. It is worth mentioning that the concept of reconfigurable antennas in this paper is different from the concept of reconfigurable antenna arrays in, e.g., [28]. As previously explained, the reconfigurable antennas are realized by changing the current flow in the antenna, while the reconfigurable antenna arrays in, e.g., [28], are achieved by changing array configurations (antenna spacings).

Although existing studies have shown that mmWave reconfigurable antennas can be realized [22–24], there still exist a number of challenges in practical implementation. In the following, we specifically discuss four issues of reconfigurable antennas that one may encounter in practical implementation, which are (1) switching delay, (2) power consumption, (3) form factor, and (4) cost. A major issue of implementing reconfigurable antennas in practice for not only sub-6 GHz systems but also mmWave communications is the switching delay incurred by changing the reconfiguration states. In practical implementation, switching the reconfigurable antennas from one state to another takes non-negligible switching time [17]. For example, a switch device with a switching time of 100 microsecond can cause considerable delays for mmWave systems. Another issue for the implementation of reconfigurable antennas is the power consumption. Compared with the traditional antennas, the reconfigurable antennas require an extra power consumption to enable the switches for reconfiguration. This issue becomes more critical considering the high power consumption of mmWave circuits and systems. The third issue for the implementation of reconfigurable antennas is their relatively large size. As the wavelength becomes small, mmWave transceivers can pack a large number of antennas in a compact size to overcome the propagation challenges. However, the employment of switches for reconfiguration makes the size of reconfigurable antennas relatively larger than traditional antennas. Thus, packing a large number of reconfigurable antennas together may result in a large form factor. Last but not least, the additional cost of circuits and switches to operate and control the antenna reconfiguration is also an issue for the implementation. In particular, the requirement of low cost would make it more challenging to address the aforementioned three issues in practical implementation.

To address the implementation issues of reconfigurable antennas, considerable research efforts on the circuit and switch designs are still needed, since the switching time, power consumption, form factor, and cost all highly depend on specific circuit topologies and switch technologies. For example, the pin diodes and MEMS switches have a relatively low power consumption and fast switching speed. However,

these devices experience larger losses at high frequencies. A possible solution is to explore smart material based switches, via metal-insulator transition compounds such as vanadium oxide (VO_2), which are designed to operate at mmWave frequencies [29]. One advantage is that smart materials do not require energy to maintain either the ON (crystalline state) or OFF (amorphous state) state, which thus reduces power consumption in switching the reconfiguration states. Also, relatively fast switching speed may be achievable by VO_2 based switches, where the demonstrated fastest switching speed is about 5 nanosecond [30].

III. SYSTEM MODEL

We consider a mmWave system where a transmitter with N_t antennas sends messages to a receiver with N_r antennas. The antennas at both the transmitter and the receiver are reconfigurable. We assume that the transmit antennas can be reconfigured into Q distinct radiation states and the receive antennas can be reconfigured into W distinct radiation states. Here two radiation states are distinct when the antenna's radiation characteristics associated with the two states are orthogonal to each other. From an electromagnetic point of view, orthogonal radiation characteristics can be generated by using polarization, pattern, space, or frequency diversity techniques, or any combination of them [15, 31–33]. For example, polarization diversity imposes orthogonality by creating orthogonal polarizations and pattern diversity imposes orthogonality by producing spatially disjoint radiation patterns. From (1), we note that one can modify the antenna's radiation characteristics $\mathbf{F}(\theta, \phi)$ by altering the antenna's physical configuration \mathbf{r}' . Thus, it is possible to have orthogonal radiation characteristics, and the numbers of distinct radiation states at the transmitter and the receiver, Q and W , correspond to the orthogonal radiation characteristics that the reconfigurable antennas can generate, which are determined by the practical circuit and antenna designs. We further assume that all the antenna ports can be reconfigured simultaneously. Then, the total number of possible combinations in which the transmit and receive ports can be reconfigured is given by $\Psi = QW$. We refer to each one of these combinations as a reconfiguration state. For brevity, we further refer to the ψ -th reconfiguration state as reconfiguration state ψ . Note that the transmitter and the receiver may have the same or different reconfiguration capabilities in practice, and our analysis is applicable to both cases by adjusting the number of radiation states at the transmitter Q and the number of radiation states at the receiver W . When $Q = W$, the transmitter and the receiver have the same reconfiguration capability. Otherwise, the transmitter and the receiver have different reconfiguration capabilities.

We consider the narrowband block-fading channels. Denote the transmitted signal vector from the transmitter as $\mathbf{x} \in \mathbb{C}^{N_t \times 1}$ with a transmit power constraint $\text{Tr}(\mathbb{E}\{\mathbf{x}\mathbf{x}^H\}) = P$. The received signal at the receiver with reconfiguration state ψ is given by

$$\mathbf{y} = \mathbf{H}_\psi \mathbf{x} + \mathbf{n}, \quad (2)$$

where $\mathbf{H}_\psi \in \mathbb{C}^{N_r \times N_t}$ denotes the channel matrix corresponding to the reconfiguration state ψ and $\mathbf{n} \sim \mathcal{CN}(\mathbf{0}; \sigma_n^2 \mathbf{I}_{N_r})$

denotes the additive white Gaussian noise (AWGN) vector at the receive antennas. Without loss of generality, the noise variance is taken to be unity, i.e., $\sigma_n^2 = 1$. Note that $\mathbf{H}_\psi(i, j)$ represents the channel coefficient that contains the gain and phase information of the path between the i -th receive antenna and the j -th transmit antenna in the reconfiguration state ψ . We assume that the channel matrices for different reconfiguration states are independent [15, 17, 25, 26], and have the same average channel power such that $\mathbb{E}\{\|\mathbf{H}_1\|_F^2\} = \dots = \mathbb{E}\{\|\mathbf{H}_\Psi\|_F^2\} = N_r N_t$. It is worth mentioning that the assumption of orthogonal radiation characteristics is crucial for our analysis, since our results are based on the assumption of independent channel matrices associated with different reconfiguration states. If the radiation patterns are non-orthogonal, the channel matrices associated with different reconfiguration states would be correlated, and we would expect a relatively smaller throughput gain compared with the results in this paper.

We further assume that full channel state information (CSI) of all reconfiguration states is known at the receiver. The full CSI is not necessarily known at the transmitter. We assume that a limited feedback from the receiver to the transmitter is available for the reconfiguration state selection and transmit beam selection, which will be detailed later in Section III-B. We would like to point out that the assumption of full CSI at the receiver or even at both the transmitter and the receiver has often been adopted in the existing papers on mmWave systems and reconfigurable antennas, see, e.g., [12, 15, 17, 25, 26, 34–38]. On the other hand, it is worth mentioning that the full CSI assumption is not easy to achieve in practice. The full CSI requires user equipments to conduct channel estimation. However, channel estimation is relatively challenging for mmWave MIMO systems. Different from sub-6 GHz systems, the precoder for mmWave MIMO with a limited number of RF chains is usually not fully digital. Due to the constrained precoding structure, the channel has to be estimated via the use of a certain number of RF beams, and each beam only presents a projection of the channel matrix rather than the full channel matrix itself. To obtain the full CSI, the channel estimation needs to be conducted over enough number of RF beams so that the full channel matrix can be estimated. The same process has to be repeatedly conducted for all the reconfiguration states as well. Thus, the channel estimation process to obtain full CSI would incur a considerable latency, and the assumption of full CSI is not easy to achieve in practice.

A. Channel Model

For low-frequency $N_r \times N_t$ MIMO systems in an ideally rich scattering environment, the channel for each reconfiguration state is usually modelled by a full rank $N_r \times N_t$ matrix with i.i.d. entries [15], e.g., i.i.d. complex Gaussian entries for Rayleigh fading channels. For mmWave communications in the clustered scattering environment, it is no longer appropriate to model the channel for each reconfiguration state as a full-rank matrix with i.i.d. entries due to the sparse nature of

mmWave channels.¹ In the following, we present the channel model of mmWave MIMO systems with reconfigurable antennas.

1) *Physical Channel Representation*: The physical channel representation is also often known as Saleh-Valenzuela (S-V) geometric model. The mmWave MIMO channel can be characterized by physical multipath models. In particular, the clustered channel representation is usually adopted as a practical model for mmWave channels [27, 39, 40]. The channel matrix for reconfiguration state ψ is contributed by $N_{\psi, \text{cl}}$ scattering clusters, and each cluster contains $N_{\psi, \text{ry}}$ propagation paths. The 2D physical multipath model for the channel matrix \mathbf{H}_ψ is given by

$$\mathbf{H}_\psi = \sum_{i=1}^{N_{\psi, \text{cl}}} \sum_{l=1}^{N_{\psi, \text{ry}}} \alpha_{\psi, i, l} \mathbf{a}_R(\theta_{\psi, i, l}^r) \mathbf{a}_T^H(\theta_{\psi, i, l}^t), \quad (3)$$

where $\alpha_{\psi, i, l}$ denotes the path gain, $\theta_{\psi, i, l}^r$ and $\theta_{\psi, i, l}^t$ denote the angle of arrival (AOA) and the angle of departure (AOD), respectively, $\mathbf{a}_R(\theta_{\psi, i, l}^r)$ and $\mathbf{a}_T^H(\theta_{\psi, i, l}^t)$ denote the steering vectors of the receive antenna array and the transmit antenna array, respectively. In this work, we consider the 1D uniform linear array (ULA) at both the transmitter and the receiver. Then, the steering vectors are given by

$$\mathbf{a}_R(\theta_{\psi, i, l}^r) = \left[1, e^{-j2\pi\vartheta_{\psi, i, l}^r}, \dots, e^{-j2\pi\vartheta_{\psi, i, l}^r(N_r-1)} \right]^T, \quad (4)$$

and

$$\mathbf{a}_T(\theta_{\psi, i, l}^t) = \left[1, e^{-j2\pi\vartheta_{\psi, i, l}^t}, \dots, e^{-j2\pi\vartheta_{\psi, i, l}^t(N_t-1)} \right]^T, \quad (5)$$

where ϑ denotes the normalized spatial angle. The normalized spatial angle is related to the physical AOA or AOD $\theta \in [-\pi/2, \pi/2]$ by $\vartheta = d \sin(\theta)/\lambda$, where d denotes the antenna spacing and λ denotes the wavelength.

We assume that $N_{1, \text{cl}} = \dots = N_{\Psi, \text{cl}}$ and $N_{1, \text{ry}} = \dots = N_{\Psi, \text{ry}}$, which implies that the sparsity of the mmWave MIMO channel remains the same for all reconfiguration states. By transmitting and receiving with orthogonal radiation patterns, the propagated signals undergo different reflections and diffractions such that different reconfiguration states lead to different multipath parameters. That is, the values of $\alpha_{\psi, i, l}$, $\theta_{\psi, i, l}^r$, and $\theta_{\psi, i, l}^t$ change as the reconfiguration state changes.

2) *Virtual Channel Representation (VCR)*: The virtual (beam-space) representation is a natural choice for modelling mmWave MIMO channels due to the highly directional nature of propagation [40]. The virtual model characterizes the physical channel by coupling between the spatial beams in fixed virtual transmit and receive directions, and represents the channel in beam-space domain.

The VCR of \mathbf{H}_ψ in (3) is given by [41, 42]

$$\begin{aligned} \mathbf{H}_\psi &= \sum_{i=1}^{N_r} \sum_{j=1}^{N_t} H_{\psi, \text{V}}(i, j) \mathbf{a}_R(\tilde{\theta}_{R, i}) \mathbf{a}_T^H(\tilde{\theta}_{T, j}) \\ &= \mathbf{A}_R \mathbf{H}_{\psi, \text{V}} \mathbf{A}_T^H, \end{aligned} \quad (6)$$

¹The existing studies on the 2×2 mmWave MIMO with reconfigurable antennas used the idealized assumption of full-rank channel matrices with i.i.d. complex Gaussian entries for all reconfiguration states, which is not practical for the general mmWave scenarios where the number of antennas is relatively large [25, 26].

where $\ddot{\theta}_{R,i} = \arcsin(\lambda \ddot{\vartheta}_{R,i}/d)$ and $\ddot{\theta}_{T,j} = \arcsin(\lambda \ddot{\vartheta}_{T,j}/d)$ are fixed virtual receive and transmit angles corresponding to uniformly spaced spatial angles²

$$\ddot{\vartheta}_{R,i} = \frac{i-1-(N_r-1)/2}{N_r} \quad (7)$$

and

$$\ddot{\vartheta}_{T,j} = \frac{j-1-(N_t-1)/2}{N_t}, \quad (8)$$

respectively,

$$\mathbf{A}_R = \frac{1}{\sqrt{N_r}} \left[\mathbf{a}_R(\ddot{\theta}_{R,1}), \dots, \mathbf{a}_R(\ddot{\theta}_{R,N_r}) \right]^T \quad (9)$$

and

$$\mathbf{A}_T = \frac{1}{\sqrt{N_t}} \left[\mathbf{a}_T(\ddot{\theta}_{T,1}), \dots, \mathbf{a}_T(\ddot{\theta}_{T,N_t}) \right]^T \quad (10)$$

are unitary DFT matrices, and $\mathbf{H}_{\psi,V} \in \mathbb{C}^{N_r \times N_t}$ is the virtual channel matrix. Since $\mathbf{A}_R \mathbf{A}_R^H = \mathbf{A}_R^H \mathbf{A}_R = \mathbf{I}_{N_r}$ and $\mathbf{A}_T \mathbf{A}_T^H = \mathbf{A}_T^H \mathbf{A}_T = \mathbf{I}_{N_t}$, the virtual channel matrix and the physical channel matrix are unitarily equivalent, such that

$$\mathbf{H}_{\psi,V} = \mathbf{A}_R^H \mathbf{H}_{\psi} \mathbf{A}_T. \quad (11)$$

3) *Low-Dimensional VCR*: For MIMO systems, the link capacity of the reconfiguration state ψ is directly related to the amount of scattering and reflection in the multipath environment. As discussed in [42, Chapter 7.3], the number of non-vanishing rows and columns of $\mathbf{H}_{\psi,V}$ depends on the amount of scattering and reflection. In the clustered scattering environment of mmWave MIMO, the dominant channel power is expected to be captured by a few rows and columns of the virtual channel matrix, i.e., a low-dimensional submatrix of $\mathbf{H}_{\psi,V}$.

The discussion above motivates the development of low-dimensional virtual representation of mmWave MIMO channels and the corresponding low-complexity beamforming designs for mmWave MIMO transceivers [28, 38, 43, 44]. Specifically, a low-dimensional virtual channel matrix, denoted by $\tilde{\mathbf{H}}_{\psi,V} \in \mathbb{C}^{L_r \times L_t}$, is obtained by beam selection from $\mathbf{H}_{\psi,V}$, such that $\tilde{\mathbf{H}}_{\psi,V}$ captures L_t dominant transmit beams and L_r dominant receive beams of the full virtual channel matrix. The low-dimensional virtual channel matrix is defined by

$$\tilde{\mathbf{H}}_{\psi,V} = [\mathbf{H}_{\psi,V}(i,j)]_{i \in \mathcal{M}_{\psi,r}, j \in \mathcal{M}_{\psi,t}}, \quad (12)$$

where $\mathcal{M}_{\psi,r} = \{i : (i,j) \in \mathcal{M}_{\psi}\}$, $\mathcal{M}_{\psi,t} = \{j : (i,j) \in \mathcal{M}_{\psi}\}$, and \mathcal{M}_{ψ} is the beam selection mask. The beam selection mask \mathcal{M} is related to the criterion of beam selection. For example, a common beam selection is based on the criterion of maximum magnitude, and the corresponding beam selection mask is defined as [43]

$$\mathcal{M}_{\psi} = \left\{ (i,j) : |\mathbf{H}_{\psi,V}(i,j)|^2 \geq \gamma_{\psi} \max_{(i,j)} |\mathbf{H}_{\psi,V}(i,j)|^2 \right\}, \quad (13)$$

where $0 < \gamma_{\psi} < 1$ is a threshold parameter used to ensure that $\tilde{\mathbf{H}}_{\psi,V}$ has the dimension of $L_r \times L_t$. Using (13), the resulting $\tilde{\mathbf{H}}_{\psi,V}$ captures a fraction γ_{ψ} of the power of $\mathbf{H}_{\psi,V}$.

Although the VCR and the beamspace hybrid beamforming for mmWave systems have been widely adopted and studied in the literature [38, 40, 43, 45–47], it is worth mentioning that there are some potential limitations on the utility of VCR in practical mmWave systems. For sub-6 GHz systems, motivated by the limitations of the S-V model and the statistical model, the intermediate VCR was introduced to keep the essence of S-V model without its complexity and to provide a tractable channel characterization [41, 48, 49]. The VCR for sub-6 GHz systems offers a simple and transparent interpretation of the effects of scattering and array characteristics [41]. However, the interpretation of VCR is based on the assumption of (approximately) unitary bases at both the transmit and the receive sides, which may not be possible in many practical mmWave systems. Note that, different from sub-6 GHz systems, mmWave systems usually do not have a large number of dominant clusters. Also, the numbers of antennas for practical mmWave transceivers are still far from the asymptotics. Thus, there may not be a solid case for the VCR in practical mmWave systems, and the statistics of the VCR for sub-6 GHz systems do not hold for mmWave systems. Consequently, the optimality of the beamspace hybrid beamforming, which is based on the VCR, in practical mmWave systems may not be easy to verify. The losses related to the application of the simple DFT and IDFT are not clear. In addition, the power leakage issue due to the beam selection may be serious in practical mmWave systems. While the DFT and IDFT are fixed, the actual angles of departure and arrival of different paths are continuously distributed. Thus, the power of a path can leak into multiple different beams [43], and selecting only a few number of beams may result in a serious issue of power loss.

B. Transceiver Architecture

For wireless communications at low frequencies, signal processing happens in the baseband, and MIMO relies on digital beamforming. At mmWave frequencies, it is difficult to employ a separate RF chain and data converter for each antenna, especially in large MIMO systems, due to the complicated hardware implementation, the high power consumption, and/or the prohibitive cost [3, 10, 12]. To reduce the number of RF chains and the number of data converters, mmWave MIMO transceivers usually have low-complexity architectures and signal processors, e.g., analog beamformer, hybrid analog-digital beamformer, and low resolution transceivers. In this work, we adopt the reconfigurable beamspace hybrid beamformer as the architecture of low-complexity transceivers for mmWave MIMO systems with reconfigurable antennas.

At the transmitter, the symbol vector $\mathbf{s} \in \mathbb{C}^{N_s \times 1}$ is first processed by a low-dimensional digital precoder $\mathbf{F} \in \mathbb{C}^{L_t \times N_s}$, where L_t denotes the number of RF chains at the transmitter. The obtained $L_t \times 1$ signal vector is denoted by $\tilde{\mathbf{x}}_V = \mathbf{F}\mathbf{s}$, which is then converted to analog signals by L_t digital-to-analog converters (DACs). Next, the L_t signals go through the beam selector to obtain the $N_t \times 1$ (virtual) signal vector \mathbf{x}_V . For a given beam selection mask \mathcal{M} , \mathbf{x}_V is constructed by $[\mathbf{x}_V(j)]_{j \in \mathcal{M}_t} = \tilde{\mathbf{x}}_V$ and $[\mathbf{x}_V(j)]_{j \notin \mathcal{M}_t} = \mathbf{0}$, where

²Without loss of generality, we here assume that N_r and N_t are odd.

$\mathcal{M}_t = \{j : (i, j) \in \mathcal{M}\}$. The beam selector can be easily realized by switches in practice. \mathbf{x}_V is further processed by the DFT analog precoder $\mathbf{A}_T \in \mathbb{C}^{N_t \times N_t}$, and the obtained signal vector is given by $\mathbf{x} = \mathbf{A}_T \mathbf{x}_V$. Note that $\text{Tr}(\mathbb{E}\{\tilde{\mathbf{x}}_V \tilde{\mathbf{x}}_V^H\}) = \text{Tr}(\mathbb{E}\{\mathbf{x}_V \mathbf{x}_V^H\}) = \text{Tr}(\mathbb{E}\{\mathbf{x} \mathbf{x}^H\}) = P$. Finally, the transmitter sends \mathbf{x} with the reconfigurable antennas.

The received signal vector at the receive antennas with a given reconfiguration state ψ is given by

$$\mathbf{y} = \mathbf{H}_\psi \mathbf{x} + \mathbf{n} = \mathbf{A}_R \mathbf{H}_{\psi,V} \mathbf{A}_T^H \mathbf{x} + \mathbf{n} = \mathbf{A}_R \mathbf{H}_{\psi,V} \mathbf{x}_V + \mathbf{n}. \quad (14)$$

At the receiver side, \mathbf{y} is first processed by the IDFT analog decoder $\mathbf{A}_R^H \in \mathbb{C}^{N_r \times N_r}$, and the obtained (virtual) signal vector is given by

$$\mathbf{y}_V = \mathbf{A}_R^H \mathbf{y} = \mathbf{H}_{\psi,V} \mathbf{x}_V + \mathbf{n}_V, \quad (15)$$

where the distribution of $\mathbf{n}_V = \mathbf{A}_R^H \mathbf{n}$ is $\mathcal{CN}(\mathbf{0}; \sigma_n^2 \mathbf{I}_{N_r})$. Note that the system representation in (15) is unitarily equivalent to the antenna domain representation in (2).

According to the given beam selection mask \mathcal{M} , the receiver then uses the beam selector to obtain the low-dimensional $L_r \times 1$ signal vector $\tilde{\mathbf{y}}_V = [\mathbf{y}_V(i)]_{i \in \mathcal{M}_r}$, where L_r denotes the number of the RF chains at the receiver and $\mathcal{M}_r = \{i : (i, j) \in \mathcal{M}\}$. The low-dimensional virtual system representation for a given reconfiguration state ψ is formulated as

$$\tilde{\mathbf{y}}_V = \tilde{\mathbf{H}}_{\psi,V} \tilde{\mathbf{x}}_V + \tilde{\mathbf{n}}_V, \quad (16)$$

where $\tilde{\mathbf{H}}_{\psi,V} = [\mathbf{H}_{\psi,V}(i, j)]_{i \in \mathcal{M}_r, j \in \mathcal{M}_t}$, $\tilde{\mathbf{n}}_V = [\mathbf{n}_V(i)]_{i \in \mathcal{M}_r}$, and $\tilde{\mathbf{n}}_V \sim \mathcal{CN}(\mathbf{0}; \sigma_n^2 \mathbf{I}_{L_r})$. The analog signals are finally converted to digital signals by L_r analog-to-digital converters (ADCs) for the low-dimensional digital signal processing.

As mentioned earlier, we assume that the full CSI is perfectly known at the receiver, and a limited feedback is available from the receiver to the transmitter to enable the beam selection and the reconfiguration state selection. Per the number of all possible combinations of selected beams and reconfiguration states, the number of the feedback bits is equal to $\log_2(\Psi) + \log_2\left(\binom{N_t}{L_t} \binom{N_r}{L_r}\right)$. We assume that $N_s = L_t \leq L_r$ to maximize the multiplexing gain of the system. The digital precoder at the transmitter is then given by $\mathbf{F} = \mathbf{I}_{N_s}$ with equal power allocation between the N_s data streams, since the transmitter does not have the full CSI. At the receiver, the digital decoder is the joint ML decoder for maximizing the throughput.³ With the aforementioned transceiver architecture and CSI assumptions, the system throughput with a selected $\tilde{\mathbf{H}}_{\psi,V}$ is given by [42]

$$R_{\tilde{\mathbf{H}}_{\psi,V}} = \log_2 \left| \mathbf{I}_{L_r} + \frac{\rho}{L_t} \tilde{\mathbf{H}}_{\psi,V} \tilde{\mathbf{H}}_{\psi,V}^H \right|, \quad (17)$$

where $\rho = P/\sigma_n^2$ denotes the transmit power to noise ratio.

IV. THROUGHPUT GAIN OF EMPLOYING RECONFIGURABLE ANTENNAS

In this section, we analyze the performance gain of employing the reconfigurable antennas in terms of the throughput.

³The relatively low-complexity MMSE-SIC decoder can also be adopted here to maximize the average throughput.

With the optimal reconfiguration state selection, the instantaneous system throughput is given by

$$R_{\hat{\psi}} = \max_{\psi \in \{1, \dots, \Psi\}} R_\psi, \quad (18)$$

where

$$\begin{aligned} R_\psi &= \log_2 \left| \mathbf{I}_{L_r} + \frac{\rho}{L_t} \hat{\mathbf{H}}_{\psi,V} \hat{\mathbf{H}}_{\psi,V}^H \right| \\ &= \max_{\tilde{\mathbf{H}}_{\psi,V} \in \{\tilde{\mathcal{H}}_\psi\}} \log_2 \left| \mathbf{I}_{L_r} + \frac{\rho}{L_t} \tilde{\mathbf{H}}_{\psi,V} \tilde{\mathbf{H}}_{\psi,V}^H \right| \end{aligned} \quad (19)$$

represents the maximum achievable throughput under the reconfiguration state ψ , $\hat{\mathbf{H}}_{\psi,V}$ denotes the optimal low-dimensional virtual channel of $\mathbf{H}_{\psi,V}$, and $\tilde{\mathcal{H}}_\psi$ denotes the set of all possible $L_r \times L_t$ submatrices of $\mathbf{H}_{\psi,V}$. Here, the optimal reconfiguration state is the reconfiguration state that maximizes the throughput.

A. Average Throughput Gain

The average throughput gain of employing the reconfigurable antennas is given by

$$G_{\bar{R}} = \bar{R}_{\hat{\psi}} / \bar{R}_\psi, \quad (20)$$

where $\bar{R}_{\hat{\psi}} = \mathbb{E}\{R_{\hat{\psi}}\}$, $\bar{R}_\psi = \mathbb{E}\{R_\psi\}$, and the expectation is over different channel realizations. As mentioned before, we assume that the channel matrices for different reconfiguration states have the same average channel power, and hence, $\bar{R}_1 = \dots = \bar{R}_\Psi$.

With the key property of VCR, each entry of $\tilde{\mathbf{H}}_{\psi,V}$, i.e., $\tilde{\mathbf{H}}_{\psi,V}(i, j)$, is associated with a set of physical paths [41], and it is approximated equal to the sum of the complex gains of the corresponding paths [28]. When the number of distinct paths associated with $\tilde{\mathbf{H}}_{\psi,V}(i, j)$ is sufficiently large, we note from the central limit theorem that $\tilde{\mathbf{H}}_{\psi,V}(i, j)$ tends toward a complex Gaussian random variable. As observed in [39] for the practical mmWave propagation environment at 60 GHz, the average number of distinct clusters is 10, and the average number of rays in each cluster is 9. The 802.11ad model has a fixed value of 18 clusters for the 60 GHz WLAN systems [50]. With the aforementioned numbers of clusters and rays, the entries of $\tilde{\mathbf{H}}_{\psi,V}$ can be approximated by zero-mean complex Gaussian variables. Different from the rich scattering environment for low-frequency communication, the associated groups of paths to different entries of $\tilde{\mathbf{H}}_{\psi,V}$ may be correlated in the mmWave environment. As a result, the entries of $\tilde{\mathbf{H}}_{\psi,V}$ can be correlated, and the entries of $\tilde{\mathbf{H}}_{\psi,V}$ are then approximated by correlated zero-mean complex Gaussian variables. In the literature, it has been shown that the instantaneous capacity of a MIMO system whose channel matrix has correlated zero-mean complex Gaussian entries can be approximated by a Gaussian variable [51, 52]. Based on the discussion above, the distribution of R_ψ is approximated by a Gaussian distribution, and the accuracy of the approximation will also be numerically shown later in Section VI. It is worth mentioning that practical mmWave channels may have relatively small numbers of clusters and paths. Different from the results in [39, 50] for 60 GHz, one may observe only

3-6 clusters at 28 GHz [53,54]. Although the distribution of $\widehat{\mathbf{H}}_{\psi,V}(i,j)$ may deviate from Gaussian when the number of distinct paths associated with it becomes small, we find that R_{ψ} is still approximately Gaussian distributed. Note that Gaussian approximated distribution for the rate of MIMO systems has been shown many times in the literature under various assumptions [51,52,55,56], and the Gaussianity of R_{ψ} with randomness in the angular profiles of the clusters is reasonable.

Denoting the approximated Gaussian distribution of R_{ψ} as $\mathcal{N}(\bar{R}_{\psi}, \sigma_{\bar{R}_{\psi}}^2)$, where \bar{R}_{ψ} and $\sigma_{\bar{R}_{\psi}}^2$ denote the mean and the variance of R_{ψ} , respectively, we have the following proposition giving the approximated average throughput gain of employing the reconfigurable antennas.

Proposition 1: The average throughput gain of employing the reconfigurable antennas with Ψ distinct reconfiguration states is approximated by

$$G_{\bar{R}} \approx \int_0^{\infty} \frac{1}{R_{\psi}} - \frac{1}{2^{\Psi} \bar{R}_{\psi}} \left(1 + \operatorname{erf} \left(\frac{x - \bar{R}_{\psi}}{\sqrt{2\sigma_{\bar{R}_{\psi}}^2}} \right) \right)^{\Psi} dx. \quad (21)$$

Proof: See Appendix A ■

To the best of our knowledge, the expression for $G_{\bar{R}}$ in (21) cannot be simplified for general values of Ψ . Thus, the calculation of the average throughput gain for a general number of reconfiguration states involves an infinite integral of a complicated function. We then further consider two special cases, in which the relatively simple expressions for the average throughput gain are tractable.

1) $\Psi \leq 5$: In practice, the number of distinct reconfiguration states is usually small, due to the complicated hardware design and the limited size of antennas. The following Corollary gives the approximated average throughput gain for the case of $\Psi \leq 5$.

Corollary 1: The approximated expressions for the average throughput gain, $G_{\bar{R}}$, for the case of $\Psi \leq 5$ are given by

$$\begin{aligned} G_{\bar{R}}(\psi = 1) &\approx 1, \quad G_{\bar{R}}(\psi = 2) \approx 1 + \frac{1}{R_{\psi}} \sqrt{\frac{\sigma_{\bar{R}_{\psi}}^2}{\pi}}, \\ G_{\bar{R}}(\psi = 3) &\approx 1 + \frac{3}{2R_{\psi}} \sqrt{\frac{\sigma_{\bar{R}_{\psi}}^2}{\pi}}, \\ G_{\bar{R}}(\psi = 4) &\approx 1 + \frac{3}{R_{\psi}} \sqrt{\frac{\sigma_{\bar{R}_{\psi}}^2}{\pi^3}} \arccos \left(-\frac{1}{3} \right), \\ G_{\bar{R}}(\psi = 5) &\approx 1 + \frac{5}{2R_{\psi}} \sqrt{\frac{\sigma_{\bar{R}_{\psi}}^2}{\pi^3}} \arccos \left(-\frac{23}{27} \right). \end{aligned} \quad (22)$$

Proof: See Appendix B ■

2) Ψ Is Large: Although Ψ is relatively small in practice, it is of theoretical importance to study the case of large Ψ to capture the limiting performance gain of reconfigurable antennas. We present the approximated average throughput gain for large Ψ in the corollary below.

Corollary 2: The approximated average throughput gain, $G_{\bar{R}}$, for the case of large Ψ is given by

$$G_{\bar{R}} \approx 1 + \frac{\sqrt{2\sigma_{\bar{R}_{\psi}}^2}}{\bar{R}_{\psi}} \left((1 - \beta) \operatorname{erf}^{-1} \left(1 - \frac{2}{\Psi} \right) + \beta \operatorname{erf}^{-1} \left(1 - \frac{2}{e\Psi} \right) \right), \quad (23)$$

where $\beta \simeq 0.5772$ denotes the Euler's constant.

Proof: See Appendix C ■

Based on (23), we further obtain the limiting behavior of the average throughput gain when Ψ becomes large in the following corollary.

Corollary 3: As $\Psi \rightarrow \infty$, $G_{\bar{R}}(\Psi)$ is asymptotically equivalent to

$$G_{\bar{R}}(\Psi) \sim \frac{\sqrt{2\sigma_{\bar{R}_{\psi}}^2}}{\bar{R}_{\psi}} \sqrt{\ln(\Psi)}. \quad (24)$$

Proof: See Appendix D ■

From (24) we find that $G_{\bar{R}}(\Psi) = O(\sqrt{\ln(\Psi)})$ as $\Psi \rightarrow \infty$. Thus, the growth of the average throughput from adding reconfiguration states becomes small when the number of reconfiguration states is already large, although having more distinct reconfiguration states always benefits the average throughput.

B. Outage Throughput Gain

In the above analysis, we focused on the performance gain in terms of the average throughput. However, it is insufficient to use the average throughput as the sole measure of the rate performance of the systems with multiple antennas. For scenarios where the channel remains (quasi) static during the transmission, it is appropriate to evaluate the system performance by the outage throughput, since every possible target transmission rate is associated with an unavoidable probability of outage. In the following, we analyze the performance gain of employing the reconfigurable antennas in terms of the outage throughput.

For a given target rate R , an outage event happens when the maximum achievable throughput is less than the target rate, and the outage probabilities for the systems without and with the reconfigurable antennas are given by $\mathbb{P}(R_{\widehat{\psi}} < R)$ and $\mathbb{P}(R_{\psi} < R)$, respectively. At a required outage level $0 < \epsilon < 1$, the outage throughputs for the systems with and without the reconfigurable antennas are given by [42]

$$R_{\widehat{\psi}}^{\text{out}} = \max R, \quad \text{s.t.} \quad \mathbb{P}(R_{\widehat{\psi}} < R) \leq \epsilon \quad (25)$$

and

$$R_{\psi}^{\text{out}} = \max R, \quad \text{s.t.} \quad \mathbb{P}(R_{\psi} < R) \leq \epsilon, \quad (26)$$

respectively. The outage throughput gain of employing the reconfigurable antennas at an outage level ϵ is given by

$$G_{R^{\text{out}}} = R_{\widehat{\psi}}^{\text{out}} / R_{\psi}^{\text{out}}, \quad (27)$$

where $R_{\widehat{\psi}}^{\text{out}}$ and R_{ψ}^{out} are given in (25) and (26), respectively. The outage throughput gain of employing the reconfigurable antennas is given in the following proposition.

Proposition 2: The outage throughput gain of employing the reconfigurable antennas with Ψ distinct reconfiguration states is approximated by

$$G_{R_{\text{out}}} \approx \frac{\bar{R}_{\psi} - \sqrt{2\sigma_{R_{\psi}}^2} \text{erf}^{-1}(1 - 2\epsilon^{\frac{1}{\Psi}})}{\bar{R}_{\psi} - \sqrt{2\sigma_{R_{\psi}}^2} \text{erf}^{-1}(1 - 2\epsilon)}. \quad (28)$$

Proof: See Appendix E ■

1) Ψ Is Large: We now investigate the limiting performance gain of reconfigurable antennas in terms of the outage throughput as $\Psi \rightarrow \infty$.

Based on (28), we present the limiting behavior of the outage throughput gain when Ψ becomes large in the following corollary.

Corollary 4: As $\Psi \rightarrow \infty$, $G_{R_{\text{out}}}(\Psi)$ is asymptotically equivalent to

$$G_{R_{\text{out}}}(\Psi) \sim \frac{\sqrt{2\sigma_{R_{\psi}}^2}}{\bar{R}_{\psi} - \sqrt{2\sigma_{R_{\psi}}^2} \text{erf}^{-1}(1 - 2\epsilon)} \sqrt{\ln(\Psi)}. \quad (29)$$

Proof: See Appendix F ■

Similar to the finding for the average throughput gain, we find from (29) that $G_{R_{\text{out}}}(\Psi) = O(\sqrt{\ln(\Psi)})$ as $\Psi \rightarrow \infty$. Thus, the growth of the outage throughput from adding reconfiguration states becomes small when the number of reconfiguration states is already large. Comparing the limiting behaviors of the average throughput gain and the outage throughput gain, we further find that the growth rate of the average throughput and the growth rate of the outage throughput have the same order when the number of reconfiguration states is large.

V. FAST SELECTION ALGORITHM

In the previous section, we analyzed the throughput gain of employing the reconfigurable antennas when the optimal reconfiguration state and beams are selected, while the problem of how to select the optimal reconfiguration state and beams has not been considered. In fact, as will be discussed later, selecting the optimal reconfiguration state and beams among all possible selections is extremely complicated and challenging for practical applications. To overcome the challenge, in this section, we propose a fast selection algorithm with low complexity and near-optimal throughput performance in the sparse mmWave MIMO environment.

The objective of selecting the optimal reconfiguration state and beams is to obtain the corresponding optimal $\tilde{\mathbf{H}}_{\psi,V}$ that maximizes the system throughput given in (17). The design problem of selecting $\tilde{\mathbf{H}}_{\psi,V}$ is formulated as⁴

$$\max_{\psi \in \{1, \dots, \Psi\}} \max_{\tilde{\mathbf{H}}_{\psi,V} \in \{\tilde{\mathcal{H}}_{\psi}\}} \left| \mathbf{I}_{L_r} + \frac{\rho}{L_t} \tilde{\mathbf{H}}_{\psi,V} \tilde{\mathbf{H}}_{\psi,V}^H \right|. \quad (30)$$

A straightforward method to obtain the optimal $\tilde{\mathbf{H}}_{\psi,V}$ is the exhaustive search among all possible selections of $\tilde{\mathbf{H}}_{\psi,V}$. That is, we first search for the optimal beam selection for each

⁴Note that the selection criteria in (30) is maximizing the throughput rather than maximizing the channel magnitude.

reconfiguration state to obtain $\hat{\tilde{\mathbf{H}}}_{\psi,V}$, i.e., the optimal low-dimensional virtual channel of $\tilde{\mathbf{H}}_{\psi,V}$. Then, we compare the obtained $\hat{\tilde{\mathbf{H}}}_{\psi,V}$ among all reconfiguration states to complete the selection of optimal $\tilde{\mathbf{H}}_{\psi,V}$, denoted by $\hat{\tilde{\mathbf{H}}}_{\hat{\psi},V}$. Since there are Ψ reconfiguration states and $\binom{N_t}{L_t} \binom{N_r}{L_r}$ possible submatrices for each state, the total number of possible selections to search is given by

$$N_{\text{total}} = \Psi \binom{N_t}{L_t} \binom{N_r}{L_r} = \frac{\Psi N_r! N_t!}{L_r! L_t! (N_r - L_r)! (N_t - L_t)!}. \quad (31)$$

When $N_t \gg L_t$, $N_r \gg L_r$, and/or $\Psi \gg 1$, the total number to search, N_{total} , would be too large for practical applications due to the high complexity. Thus, in what follows, we propose a low-complexity design to obtain $\hat{\tilde{\mathbf{H}}}_{\hat{\psi},V}$ which achieves the near optimal throughput performance.

As discussed earlier, the mmWave MIMO channel has a sparse nature, and the number of non-vanishing rows and columns of the virtual channel matrix is relatively small in the clustered scattering environment. Now let us consider an extreme scenario such that all of the non-vanishing entries of $\mathbf{H}_{\psi,V}$ are contained in the low-dimensional submatrix, and $\mathbf{H}_{\psi,V}$ is approximated by

$$\mathbf{M} \odot \mathbf{H}_{\psi,V}, \quad (32)$$

where

$$\mathbf{M}(i, j) = \begin{cases} 1, & \text{if } (i, j) \in \hat{\mathcal{M}}_{\psi}, \\ 0, & \text{otherwise,} \end{cases} \quad (33)$$

and $\hat{\mathcal{M}}_{\psi}$ is the beam selection mask corresponding to $\hat{\tilde{\mathbf{H}}}_{\psi,V}$. Note that a similar approximation was adopted in, e.g., [28] to approximate the sparse virtual MIMO channel. With (32), we have

$$\begin{aligned} \left| \mathbf{I}_{L_r} + \frac{\rho}{L_t} \hat{\tilde{\mathbf{H}}}_{\psi,V} \hat{\tilde{\mathbf{H}}}_{\psi,V}^H \right| &\approx \left| \mathbf{I}_{N_r} + \frac{\rho}{L_t} \mathbf{H}_{\psi,V} \mathbf{H}_{\psi,V}^H \right| \\ &= \left| \mathbf{I}_{N_r} + \frac{\rho}{L_t} \mathbf{H}_{\psi} \mathbf{H}_{\psi}^H \right|. \end{aligned} \quad (34)$$

Based on (34), we find that a fast selection of reconfiguration state can be achieved by directly comparing their (full) physical channel matrices. Instead of finding the optimal beam selection of each reconfiguration state first, we can directly determine the optimal reconfiguration state by

$$\hat{\psi} = \arg \max_{\psi \in \{1, \dots, \Psi\}} \left| \mathbf{I}_{N_r} + \frac{\rho}{L_t} \mathbf{H}_{\psi} \mathbf{H}_{\psi}^H \right|. \quad (35)$$

Based on (35), the near-optimal reconfiguration state can be selected by calculating and comparing the throughput among only Ψ possible channel matrices. Note that \mathbf{H}_{ψ} in (35) is the full channel matrix rather than a low-dimensional virtual channel matrix associated with a particular selection of beams. In addition, with the fast reconfiguration state selection, we can select beams from only the beams that are associated with the selected reconfiguration state. In contrast, the exhaustive search needs to examine the performance of all beams associated with all reconfigurable states. Although the performance of this fast-selection method depends on the accuracy of the

approximation in (32), we will show later by numerical results that usually near optimal performance can be achieved.

To reduce the complexity of beam selection, we utilize the technique of separate transmit and receive antenna selection [57] and the incremental successive selection algorithm (ISSA) [58]. Again due to the sparsity of mmWave channels, the dominant beams usually significantly outperform the other beams, and they can be easily selected by the fast beam selection scheme. Note that the transmitter does not have the full CSI in the considered system, and hence, the existing beamspace selection schemes in, e.g., [38], with the requirement of full CSI on the beamspace channel at the transmitter are not applicable in our work. Our fast beam selection method is explained next. The beam selection problem in fact includes both transmit and receive beam selections. We adopt a separate transmit and receive beam selection technique [57] for first selecting the best L_r receive beams and then selecting the best L_t transmit beams. For both the receive and transmit beam selections, a technique based on the incremental successive selection algorithm (ISSA) [58] is utilized. We start from the empty set of selected beams, and then successively add an individual beam to this set at each step of the beam selection algorithm until the number of selected transmit and receive beams reach L_t and L_r , respectively. Note that successively selecting one beam at each step for the algorithm does not mean that we successively turn on individual beams. Instead, we first determine the set of selected beams by successively

Algorithm 1 Fast Selection

```

1: procedure FASTSELALG( $\rho, N_r, N_t, L_r, L_t, \mathbf{H}_1, \dots, \mathbf{H}_\Psi$ )
2:    $\hat{\psi} := \arg \max_{\psi \in \{1, \dots, \Psi\}} \left[ \mathbf{I}_{N_r} + \frac{\rho}{L_t} \mathbf{H}_\psi \mathbf{H}_\psi^H \right]$ ;
3:    $\mathcal{I}_r := \{1, \dots, N_r\}$ ;  $\mathcal{I}_t := \{1, \dots, N_t\}$ ;  $\mathbf{h}_j := j$ -th row of  $\mathbf{H}_{\hat{\psi}, V}$ ,  $\forall j \in \mathcal{I}_r$ ;
4:    $J := \arg \max_{j \in \mathcal{I}_r} \mathbf{h}_j \mathbf{h}_j^H$ ;
5:    $\mathcal{M}_r := \{J\}$ ;  $\tilde{\mathbf{H}}_{\hat{\psi}, V} := \left[ \mathbf{H}_{\hat{\psi}, V}(i, j) \right]_{i \in \mathcal{M}_r, j \in \mathcal{I}_t}$ ;  $\mathcal{I}_r := \mathcal{I}_r - \{J\}$ ;
6:   for  $l := 2 : L_r$  do
7:      $J := \arg \max_{j \in \mathcal{I}_r} \mathbf{h}_j \left( \mathbf{I}_{N_t} + \frac{\rho}{N_t} \tilde{\mathbf{H}}_{\hat{\psi}, V}^H \tilde{\mathbf{H}}_{\hat{\psi}, V} \right)^{-1} \mathbf{h}_j^H$ ;
8:      $\mathcal{M}_r := \mathcal{M}_r + \{J\}$ ;  $\tilde{\mathbf{H}}_{\hat{\psi}, V} := \left[ \mathbf{H}_{\hat{\psi}, V}(i, j) \right]_{i \in \mathcal{M}_r, j \in \mathcal{I}_t}$ ;
9:      $\mathcal{I}_r := \mathcal{I}_r - \{J\}$ ;
10:  end for
11:   $\mathbf{h}_j := j$ -th column of  $\tilde{\mathbf{H}}_{\hat{\psi}, V}$ ,  $\forall j \in \mathcal{I}_t$ ;
12:   $J := \arg \max_{j \in \mathcal{I}_r} \mathbf{h}_j^H \mathbf{h}_j$ ;
13:   $\mathcal{M}_t := \{J\}$ ;  $\hat{\mathbf{H}}_{\hat{\psi}, V} := \left[ \tilde{\mathbf{H}}_{\hat{\psi}, V}(i, j) \right]_{i \in \mathcal{M}_r, j \in \mathcal{M}_t}$ ;  $\mathcal{I}_t := \mathcal{I}_t - \{J\}$ ;
14:  for  $l := 2 : L_t$  do
15:     $J := \arg \max_{j \in \mathcal{I}_t} \mathbf{h}_j^H \left( \mathbf{I}_{L_r} - \frac{\rho}{L_t} \hat{\mathbf{H}}_{\hat{\psi}, V} \left( \mathbf{I}_{l-1} + \frac{\rho}{L_t} \hat{\mathbf{H}}_{\hat{\psi}, V}^H \hat{\mathbf{H}}_{\hat{\psi}, V} \right)^{-1} \hat{\mathbf{H}}_{\hat{\psi}, V}^H \right) \mathbf{h}_j$ ;
16:     $\mathcal{M}_t := \mathcal{M}_t + \{J\}$ ;  $\hat{\mathbf{H}}_{\hat{\psi}, V} := \left[ \hat{\mathbf{H}}_{\hat{\psi}, V}(i, j) \right]_{i \in \mathcal{M}_r, j \in \mathcal{M}_t}$ ;
17:     $\mathcal{I}_t := \mathcal{I}_t - \{J\}$ ;
18:  end for
19:  return  $\hat{\psi}, \mathcal{M}_r, \mathcal{M}_t, \hat{\mathbf{H}}_{\hat{\psi}, V}$ ;
20: end procedure

```

selecting beams according to the algorithm. After determining the set of selected beams, the transmitter and the receiver selectively turn on all selected beams together by beam selectors [40, 43]. In each step of the algorithm, the objective is to select one of the unselected beams that leads to the highest increase of the throughput. The mechanism of ISSA-based receive beam selection is provided as follows. Denote the submatrix corresponding to the selected n receive beams after n steps of ISSA as $\tilde{\mathbf{H}}_{\psi, V}^n \in \mathbb{C}^{n \times N_t}$ and the j -th row of $\mathbf{H}_{\psi, V}$ by $\mathbf{h}_{\psi, V}^j$. Since the contribution of the j -th receive beam to the throughput under the log function is given by

$$g_{\psi, n, j} = \mathbf{h}_{\psi, V}^j \left(\mathbf{I}_{N_t} + \frac{\rho}{N_t} \left(\tilde{\mathbf{H}}_{\psi, V}^n \right)^H \tilde{\mathbf{H}}_{\psi, V}^n \right)^{-1} \left(\mathbf{h}_{\psi, V}^j \right)^H, \quad (36)$$

we select the receive beam at the $n + 1$ step by

$$\mathbf{h}_{\psi, V}^J = \arg \max_{\mathbf{h}_{\psi, V}^j} g_{\psi, n, j}. \quad (37)$$

The mechanism of ISSA-based transmit beam selection is omitted here, since it is similar to that of the ISSA-based receive beam selection.

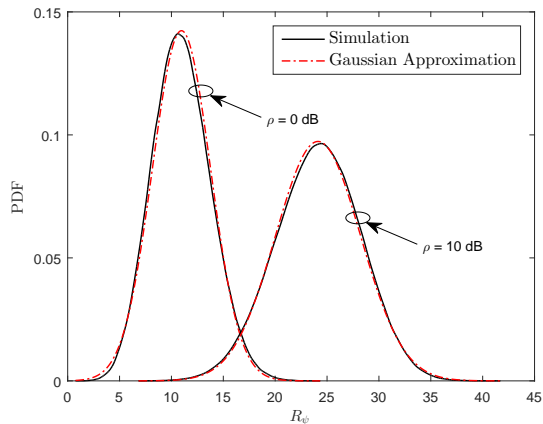
The proposed fast selection algorithm is given as Algorithm 1. The outputs of the algorithm are the optimal reconfiguration state, the indices of the selected receive beams, the indices of the selected transmit beams, and the selected low-dimensional virtual channel, denoted by $\hat{\psi}$, \mathcal{M}_r , \mathcal{M}_t , and $\hat{\mathbf{H}}_{\hat{\psi}, V}$, respectively.

We would like to highlight that the proposed algorithm significantly reduces the complexity of reconfiguration state selection and beam selection, and achieves the near-optimal throughput performance. It is worth pointing out that an important requirement of the proposed algorithm is the knowledge of full CSI of all reconfigurable states, and the associated channel estimation complexity has not been taken into account. Although the full CSI assumption has been widely-adopted in the literature, as mentioned earlier, the channel estimation is relatively challenging for mmWave systems with reconfigurable antennas.

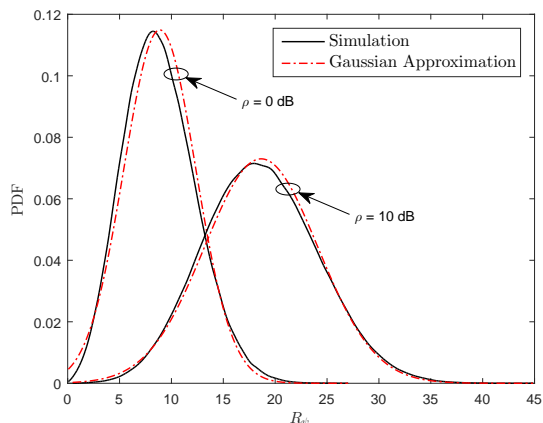
VI. NUMERICAL RESULTS

For all numerical results in this work, we adopt the clustered multipath channel model in (3) to generate the channel matrix. We assume that $\alpha_{\psi, i, l}$ are i.i.d. $\mathcal{CN}(0, \sigma_{\alpha, \psi, i}^2)$, where $\sigma_{\alpha, \psi, i}^2$ denotes the average power of the i -th cluster, and $\sum_{i=1}^{N_{\psi, c}} \sigma_{\alpha, \psi, i}^2 = \gamma_{\psi}$, where γ_{ψ} is a normalization parameter to ensure that $\mathbb{E}\{\|\mathbf{H}_{\psi}\|^2\} = N_r N_t$. We also assume that $\theta_{\psi, i, l}^r$ are uniformly distributed with mean $\theta_{\psi, i}^r$ and a constant angular spread (standard deviation) σ_{θ^r} . $\theta_{\psi, i, l}^t$ are uniformly distributed with mean $\theta_{\psi, i}^t$ and a constant angular spread (standard deviation) σ_{θ^t} . We further assume that $\theta_{\psi, i}^r$ and $\theta_{\psi, i}^t$ are both uniformly distributed within the range of $[-\pi/2, \pi/2]$. Unless otherwise stated, the system parameters are $N_r = N_t = 17$, $L_r = L_t = 5$, $N_{\psi, \text{cl}} = 10$, $N_{\psi, \text{ry}} = 8$, $\sigma_{\theta^r} = \sigma_{\theta^t} = 3^\circ$, and $d/\lambda = 1/2$. All average results are over 5,000 randomly generated channel realizations. Note that $N_{\psi, \text{cl}} = 10$ and $N_{\psi, \text{ry}} = 8$ are based on the existing

observations at 60 GHz in the literature [39, 50], and practical mmWave channels at 28 GHz may have relatively small numbers of clusters and paths [53, 54].



(a) $N_{\psi,cl} = 10, N_{\psi,ry} = 8.$



(b) $N_{\psi,cl} = 4, N_{\psi,ry} = 2.$

Fig. 1: PDF of R_{ψ} . The parameters are $N_r = N_t = 17, L_r = L_t = 5, \sigma_{\theta r} = \sigma_{\theta t} = 3^\circ$, and $d/\lambda = 1/2$.

We first demonstrate the accuracy of the Gaussian approximated probability density function (PDF) of R_{ψ} . Figure 1 plots the simulated PDF and the Gaussian approximated PDF of R_{ψ} . Figure 1(a) and Figure 1(b) are for the case of $N_{\psi,cl} = 10$ and $N_{\psi,ry} = 8$ and the case of $N_{\psi,cl} = 4$ and $N_{\psi,ry} = 2$, respectively. Different transmit power to noise ratios are considered, i.e., $\rho = 0$ dB and $\rho = 10$ dB. The transmit powers of 30 dBm and 40 dBm are considered based on the existing studies on mmWave systems [3, 27, 59]. We note that the Gaussian approximations match the simulated PDFs. In particular, we observe from Figure 1(b) that the distribution of R_{ψ} can be well approximated by the Gaussian distribution even for relatively small numbers of clusters and paths.

We then show the average throughput gain of employing the reconfigurable antennas. Figure 2 plots the average throughput gain, $G_{\bar{R}}$, versus the number of reconfiguration states, Ψ . The illustrated results are for the actual gain in (20) by simulating the channels, \mathbf{H}_{ψ} , the theoretical approximation in (21), the simplified theoretical approximation for $\Psi \leq 5$ in (22), and

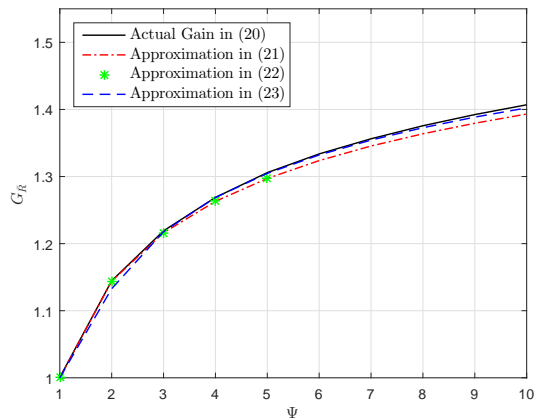


Fig. 2: Average throughput gain versus number of reconfiguration states. The parameters are $\rho = 0$ dB, $N_r = N_t = 17, L_r = L_t = 5, N_{\psi,cl} = 10, N_{\psi,ry} = 8, \sigma_{\theta r} = \sigma_{\theta t} = 3^\circ$, and $d/\lambda = 1/2$.

the simplified theoretical approximation for large Ψ in (23). As depicted in the figure, the derived theoretical approximations match precisely the simulated results. In particular, we note that the simplified approximation for large Ψ in (23) has good accuracy even when Ψ is small. From all four curves, we find that the growth of $G_{\bar{R}}$ with Ψ is fast when Ψ is small, while it becomes slow when Ψ is relatively large. This finding is consistent with the analysis in Section IV-A, and it indicates that the dominant average throughput gain of employing the reconfigurable antennas can be achieved by having a few number of reconfiguration states.

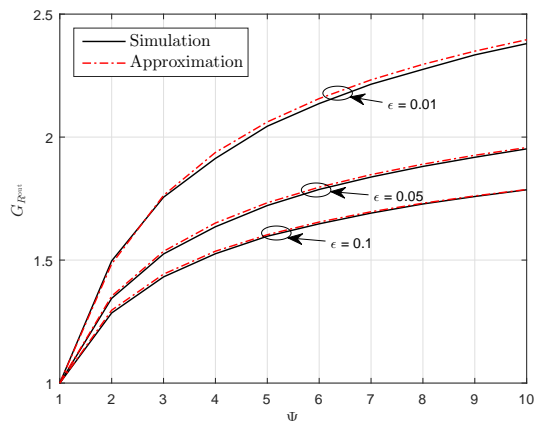


Fig. 3: Outage throughput gain versus number of reconfiguration states. The parameters are $\rho = 0$ dB, $N_r = N_t = 17, L_r = L_t = 5, N_{\psi,cl} = 10, N_{\psi,ry} = 8, \sigma_{\theta r} = \sigma_{\theta t} = 3^\circ$, and $d/\lambda = 1/2$.

We now present the outage throughput gain of employing the reconfigurable antennas. Figure 3 plots the outage throughput gain, $G_{R^{out}}$, versus the number of reconfiguration states, Ψ . Different outage levels are considered, i.e., $\epsilon = 0.01, \epsilon = 0.05$, and $\epsilon = 0.1$. As the figure shows, $G_{R^{out}}$ increases as Ψ increases. Similar to the results in Figure 2, we find that the dominant outage throughput gain of employing the reconfigurable antennas can be achieved by having a few number of reconfiguration states. To obtain the

outage throughput gain of $G_{R^{\text{out}}} = 1.5$, we only need $\Psi = 2$, $\Psi = 3$, and $\Psi = 4$ reconfiguration states for the systems requiring $\epsilon = 0.01$, $\epsilon = 0.05$, and $\epsilon = 0.1$, respectively. In addition, we note that $G_{R^{\text{out}}}$ increases as ϵ increases, which indicates that the outage throughput gain of employing the reconfigurable antennas is more significant when the required outage level becomes more stringent.

Finally, we examine the performance of the proposed algorithm for fast selection by evaluating the average throughput loss ratio, which is defined by

$$\Delta_R = (\bar{R}_{\text{max}} - \bar{R}_{\text{fast}}) / \bar{R}_{\text{opt}}, \quad (38)$$

where \bar{R}_{max} denotes the average throughput achieved by the exhaustive search and \bar{R}_{fast} denotes the average throughput achieved by the proposed fast selection algorithm. Figure 4 plots the throughput loss ratio, Δ_R , versus the transmit power to noise ratio, ρ . Systems with different numbers of reconfiguration states are considered, i.e., $\Psi = 2$, $\Psi = 4$, and $\Psi = 8$. As shown in the figure, the proposed fast selection algorithm achieves reasonably good performance compared with the maximum achievable throughput by the exhaustive search. Although Δ_R increases as Ψ increases, the throughput loss ratio is less than 3.5% even when $\Psi = 8$.

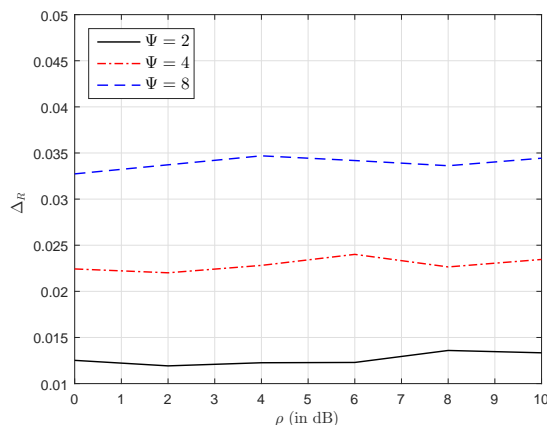


Fig. 4: Average throughput loss ratio versus transmit power to noise ratio. The parameters are $N_r = N_t = 17$, $L_r = L_t = 5$, $N_{\psi, \text{cl}} = 10$, $N_{\psi, \text{ry}} = 8$, $\sigma_{\theta r} = \sigma_{\theta t} = 3^\circ$, and $d/\lambda = 1/2$.

VII. CONCLUSIONS AND FUTURE WORK

In this paper, we have presented a framework for the theoretical study of the mmWave MIMO with reconfigurable antennas, where the low-complexity transceivers and the sparse channels are considered. We have shown that employing reconfigurable antennas can provide both the average throughput gain and the outage throughput gain for mmWave MIMO systems. Also, we have derived the approximated expressions for the gains. Based on the highly sparse nature of mmWave channels, we have further developed a fast algorithm for reconfiguration state selection and beam selection. The accuracy of our derived expressions and the performance of the developed algorithm have been verified by numerical results. We have noted from the results that the dominant throughput gains by employing the reconfigurable antennas can be achieved

by having a few number of reconfiguration states. Numerical results have shown that a system with 3 reconfiguration states can achieve an average throughput gain of 1.2 and an outage throughput gain of 1.5 for an outage requirement of $\epsilon = 0.05$.

As a first comprehensive study on the mmWave MIMO with reconfigurable antennas, our paper can lead to a number of future research directions in this area. In this paper, we have only considered the distinct reconfiguration states with independent channel matrices. In practice, the reconfiguration states may be dependent due to the non-orthogonal radiation characteristics, and the associated channel matrices may be correlated. Thus, taking the dependent reconfiguration states into consideration is an interesting future work, where we can have correlated and non-identically distributed R_{ψ} . While this paper has adopted the VCR as the analytical channel model, as mentioned earlier, there are some potential limitations on the utility of VCR in practical mmWave systems. Thus, investigating the reconfigurable antennas for mmWave systems with other channel models, e.g., the S-V model, is an important and interesting future work. Furthermore, future work on effective channel estimation techniques with low latency for mmWave systems with reconfigurable antennas is needed. Also, the associated complexity of channel estimation needs to be taken into account for future system designs. For example, if the channel matrices associated with different reconfiguration states are (strongly) correlated, a potential scheme for reconfiguration state selection and beam selection requiring a low-complexity channel estimation may start by setting the reconfiguration state to a random initial state. After finding the optimal beams in the initial state, one can reselect another state based on the optimal beams for the initial state.

APPENDIX A

PROOF OF PROPOSITION 1

With the Gaussian approximation of the distribution of R_{ψ} , we can then approximate R_{ψ} as the maximum of Ψ i.i.d. Gaussian random variables, and

$$\begin{aligned} \bar{R}_{\psi} &\approx \int_0^{\infty} 1 - (F_{R_{\psi}}(x))^{\Psi} dx \\ &= \int_0^{\infty} 1 - \frac{1}{2^{\Psi}} \left(1 + \operatorname{erf} \left(\frac{x - \bar{R}_{\psi}}{\sqrt{2\sigma_{R_{\psi}}^2}} \right) \right)^{\Psi} dx, \end{aligned} \quad (39)$$

where

$$F_{R_{\psi}}(x) = 1 + \operatorname{erf} \left(\frac{x - \bar{R}_{\psi}}{\sqrt{2\sigma_{R_{\psi}}^2}} \right) \quad (40)$$

denotes the approximated cdf of R_{ψ} .

Substituting (39) into (20) completes the proof.

APPENDIX B

PROOF OF COROLLARY 1

We rewrite $G_{\bar{R}}$ as

$$G_{\bar{R}}(\Psi = i) \approx 1 + \frac{\sqrt{\sigma_{R_{\psi}}^2}}{\bar{R}_{\psi}} E_i, \quad (41)$$

where E_i denotes the mean of the maximum of i independent standard normal random variables. Denoting the cdf of standard normal distribution by $\Phi(\cdot)$, we have

$$\begin{aligned} E_i &= \int_{-\infty}^{\infty} x \frac{d(\Phi(x))^i}{dx} dx \\ &= i(i-1) \int_{-\infty}^{\infty} \frac{\exp(-x^2)}{2\pi} (\Phi(x))^{i-2} dx \\ &= \frac{i(i-1)}{2\pi} \sum_{j=0}^{\lfloor \frac{i-1}{2} \rfloor} \left(\frac{1}{2}\right)^{i-2-2j} \binom{i-2}{2j} A_j, \end{aligned} \quad (42)$$

where $A_j = \int_{-\infty}^{\infty} \exp(-x^2) (\Phi(x) - \frac{1}{2})^{2j} dx$. We note that A_0 and A_1 can be derived⁵, which are given by $A_0 = \sqrt{\pi}$ and $A_1 = \frac{1}{2\sqrt{\pi} \tan^{-1}(\frac{\sqrt{2}}{4})}$, respectively. Substituting A_0 and A_1 into (42), we can obtain $E_1 = 0$, $E_2 = \pi^{-\frac{1}{2}}$, $E_3 = \frac{3}{2}\pi^{-\frac{1}{2}}$, $E_4 = 3\pi^{-\frac{3}{2}} \arccos(-\frac{1}{3})$, and $E_5 = \frac{5}{2}\pi^{-\frac{3}{2}} \arccos(-\frac{23}{27})$. Finally, substituting the expressions for E_1, \dots, E_5 into (41) completes the proof.

APPENDIX C PROOF OF COROLLARY 2

When Ψ is large, we can adopt the Fisher-Tippett theorem to approximate the distribution of the maximum of Ψ independent standard normal random variables as a Gumbel distribution, whose cumulative distribution function (cdf) is given by

$$F_{E_\Psi}(x) = \exp\left(-\exp\left(-\frac{x - \Phi^{-1}\left(1 - \frac{1}{\Psi}\right)}{\Phi^{-1}\left(1 - \frac{1}{e\Psi}\right) - \Phi^{-1}\left(1 - \frac{1}{\Psi}\right)}\right)\right), \quad (43)$$

where $\Phi^{-1}(\cdot)$ denotes the inverse cdf of the standard normal distribution. We then have

$$E_\Psi \approx \sqrt{2} \left((1-\beta) \operatorname{erf}^{-1}\left(1 - \frac{2}{\Psi}\right) + \beta \operatorname{erf}^{-1}\left(1 - \frac{2}{e\Psi}\right) \right), \quad (44)$$

where β denotes the Euler's constant. Substituting (44) into (41) completes the proof.

APPENDIX D PROOF OF COROLLARY 3

From the tail region approximation for the inverse error function, we note that

$$\operatorname{erf}^{-1}(x) = \sqrt{-\ln(1-x^2)} \quad \text{as } x \rightarrow 1. \quad (45)$$

⁵The detailed steps to derive A_0 and A_1 are omitted here. The interested reader can find a relevant discussion at <https://math.stackexchange.com/questions/473229>.

Based on (45) and (23), as $\Psi \rightarrow \infty$, $G_{\bar{R}}(\Psi)$ is asymptotically equivalent to

$$\begin{aligned} G_{\bar{R}}(\Psi) &\sim 1 + \frac{\sqrt{2\sigma_{R_\psi}^2}}{R_\psi} \left((1-\beta) \sqrt{-\ln(4) + \ln\left(\frac{\Psi^2}{\Psi-1}\right)} \right. \\ &\quad \left. + \beta \sqrt{1 - \ln(4) + \ln\left(\frac{\Psi^2}{\Psi-1/e}\right)} \right) \\ &\sim \frac{\sqrt{2\sigma_{R_\psi}^2}}{\bar{R}_\psi} \sqrt{\ln(\Psi)}. \end{aligned} \quad (46)$$

This completes the proof.

APPENDIX E PROOF OF PROPOSITION 2

With the Gaussian approximated PDF of R_ψ , we have the approximated outage probabilities for the systems without and with reconfigurable antennas as

$$\mathbb{P}(R_\psi < R) = F_{R_\psi}(R) \quad (47)$$

and

$$\mathbb{P}(R_{\hat{\psi}} < R) = (F_{R_\psi}(R))^\Psi, \quad (48)$$

respectively, where $F_{R_\psi}(x)$ is given in (40). Substituting (47) and (48) into (25) and (26), respectively, we can obtain the approximated $R_{\hat{\psi}}^{\text{out}}$ and R_ψ^{out} as

$$R_{\hat{\psi}}^{\text{out}} \approx F_{R_\psi}^{-1}(\epsilon^{\frac{1}{\Psi}}) = \bar{R}_\psi - \sqrt{2\sigma_{R_\psi}^2} \operatorname{erf}^{-1}\left(1 - 2\epsilon^{\frac{1}{\Psi}}\right) \quad (49)$$

and

$$R_\psi^{\text{out}} \approx F_{R_\psi}^{-1}(\epsilon) = \bar{R}_\psi - \sqrt{2\sigma_{R_\psi}^2} \operatorname{erf}^{-1}(1 - 2\epsilon), \quad (50)$$

respectively, where $F_{R_\psi}^{-1}(x)$ denotes the approximated inverse cdf of R_ψ .

Substituting (49) and (50) into (27) completes the proof.

APPENDIX F PROOF OF COROLLARY 4

As $\Psi \rightarrow \infty$, we have $1 - 2\epsilon^{\frac{1}{\Psi}} \rightarrow -1$. From the tail region approximation for the inverse error function, we note that

$$\operatorname{erf}^{-1}(x) = -\sqrt{-\ln(1-x^2)} \quad \text{as } x \rightarrow -1. \quad (51)$$

Based on (51) and (23), as $\Psi \rightarrow \infty$, $G_{R^{\text{out}}}(\Psi)$ is asymptotically equivalent to

$$\begin{aligned} G_{R^{\text{out}}}(\Psi) &\sim \frac{\bar{R}_\psi}{\bar{R}_\psi - \sqrt{2\sigma_{R_\psi}^2} \operatorname{erf}^{-1}(1 - 2\epsilon)} + \\ &\quad \frac{\sqrt{2\sigma_{R_\psi}^2}}{\bar{R}_\psi - \sqrt{2\sigma_{R_\psi}^2} \operatorname{erf}^{-1}(1 - 2\epsilon)} \sqrt{-\ln\left(1 - \left(1 - 2\epsilon^{\frac{1}{\Psi}}\right)^2\right)} \\ &\sim \frac{\sqrt{2\sigma_{R_\psi}^2}}{\bar{R}_\psi - \sqrt{2\sigma_{R_\psi}^2} \operatorname{erf}^{-1}(1 - 2\epsilon)} \sqrt{-\ln\left(1 - \epsilon^{\frac{1}{\Psi}}\right)} \\ &\stackrel{(a)}{\sim} \frac{\sqrt{2\sigma_{R_\psi}^2}}{\bar{R}_\psi - \sqrt{2\sigma_{R_\psi}^2} \operatorname{erf}^{-1}(1 - 2\epsilon)} \sqrt{\ln(\Psi)}, \end{aligned} \quad (52)$$

where (a) is derived by analyzing the Taylor series of $\sqrt{-\ln(1-\epsilon^{\frac{1}{\Psi}})}$ at $\Psi \rightarrow \infty$. This completes the proof.

REFERENCES

- [1] B. He and H. Jafarkhani, "Millimeter wave communications with reconfigurable antennas," in *Proc. IEEE ICC*, May 2018. [Online]. Available: <http://arxiv.org/abs/1806.00051>
- [2] T. S. Rappaport, R. W. Heath, R. C. Daniels, and J. N. Murdock, *Millimeter Wave Wireless Communications*. Prentice Hall, 2014.
- [3] Z. Pi and F. Khan, "An introduction to millimeter-wave mobile broadband systems," *IEEE Commun. Mag.*, vol. 49, no. 6, pp. 101–107, June 2011.
- [4] 3GPP, "Study on channel model for frequencies from 0.5 to 100 GHz," 3rd Generation Partnership Project (3GPP), Tech. Rep. TR 38.901 V14.1.1, Aug. 2017.
- [5] —, "Technical specification group radio access network; channel model for frequency spectrum above 6 GHz," 3rd Generation Partnership Project (3GPP), Tech. Rep. TR 38.900 V14.2.0, Dec. 2016.
- [6] —, "New measurements at 24 GHz in a rural macro environment," Telstra, Ericsson, Tech. Rep. TDOC R1-164975, May 2016.
- [7] T. S. Rappaport, S. Sun, R. Mayzus, H. Zhao, Y. Azar, K. Wang, G. N. Wong, J. K. Schulz, M. Samimi, and F. Gutierrez, "Millimeter wave mobile communications for 5G cellular: It will work!" *IEEE Access*, vol. 1, pp. 335–349, May 2013.
- [8] J. Kim and I. Lee, "802.11 WLAN: history and new enabling MIMO techniques for next generation standards," *IEEE Commun. Mag.*, vol. 53, no. 3, pp. 134–140, Mar. 2015.
- [9] Q. Li, G. Li, W. Lee, M. i. Lee, D. Mazzaresse, B. Clerckx, and Z. Li, "MIMO techniques in WiMAX and LTE: a feature overview," *IEEE Commun. Mag.*, vol. 48, no. 5, pp. 86–92, May 2010.
- [10] C. H. Doan, S. Emami, D. A. Sobel, A. M. Niknejad, and R. W. Brodersen, "Design considerations for 60 GHz CMOS radios," *IEEE Commun. Mag.*, vol. 42, no. 12, pp. 132–140, Dec. 2004.
- [11] V. Venkateswaran and A. J. van der Veen, "Analog beamforming in MIMO communications with phase shift networks and online channel estimation," *IEEE Trans. Signal Process.*, vol. 58, no. 8, pp. 4131–4143, Aug. 2010.
- [12] O. E. Ayach, S. Rajagopal, S. Abu-Surra, Z. Pi, and R. W. Heath, "Spatially sparse precoding in millimeter wave MIMO systems," *IEEE Transactions on Wireless Communications*, vol. 13, no. 3, pp. 1499–1513, Mar. 2014.
- [13] L. Liu and H. Jafarkhani, "Space-time trellis codes based on channel-phase feedback," *IEEE Trans. Commun.*, vol. 54, no. 12, pp. 2186–2198, Dec. 2006.
- [14] B. A. Cetiner, H. Jafarkhani, J.-Y. Qian, H. J. Yoo, A. Grau, and F. D. Flaviis, "Multifunctional reconfigurable MEMS integrated antennas for adaptive MIMO systems," *IEEE Commun. Mag.*, vol. 42, no. 12, pp. 62–70, Dec. 2004.
- [15] A. Grau, H. Jafarkhani, and F. D. Flaviis, "A reconfigurable multiple-input multiple-output communication system," *IEEE Trans. Wireless Commun.*, vol. 7, no. 5, pp. 1719–1733, May 2008.
- [16] C. A. Balanis, *Antenna Theory: Analysis and Design*, 3rd ed. Wiley, 2005.
- [17] F. Fazel, A. Grau, H. Jafarkhani, and F. D. Flaviis, "Space-time-state block coded MIMO communication systems using reconfigurable antennas," *IEEE Trans. Wireless Commun.*, vol. 8, no. 12, pp. 6019–6029, Dec. 2009.
- [18] C. G. Christodoulou, Y. Tawk, S. A. Lane, and S. R. Erwin, "Reconfigurable antennas for wireless and space applications," *Proc. IEEE*, vol. 100, no. 7, pp. 2250–2261, July 2012.
- [19] R. L. Haupt and M. Lanagan, "Reconfigurable antennas," *IEEE Antennas Propag. Mag.*, vol. 55, no. 1, pp. 49–61, Feb. 2013.
- [20] S. Pendharker, R. K. Shevgaonkar, and A. N. Chandorkar, "Optically controlled frequency-reconfigurable microstrip antenna with low photo-conductivity," *IEEE Antennas Wireless Propag. Lett.*, vol. 13, pp. 99–102, Jan. 2014.
- [21] H. Jafarkhani, *Space-Time Coding: Theory and Practice*. Cambridge University Press, 2005.
- [22] S. F. Jilani, B. Greinke, Y. Hao, and A. Alomainy, "Flexible millimeter-wave frequency reconfigurable antenna for wearable applications in 5G networks," in *Proc. URSI EMTS*, Aug. 2016, pp. 846–848.
- [23] B. Ghassemiparvin and N. Ghalichechian, "Reconfigurable millimeter-wave antennas using paraffin phase change materials," in *Proc. EuCAP*, Apr. 2016, pp. 1–4.
- [24] I. F. da Costa, A. C. S., D. H. Spadoti, L. G. da Silva, J. A. J. Ribeiro, and S. E. Barbin, "Optically controlled reconfigurable antenna array for mm-wave applications," *IEEE Antennas Wireless Propag. Lett.*, vol. 16, pp. 2142–2145, May 2017.
- [25] V. Vakilian, H. Mehrpouyan, and Y. Hua, "High rate space-time codes for millimeter-wave systems with reconfigurable antennas," in *Proc. IEEE WCNC*, Mar. 2015, pp. 591–596.
- [26] V. Vakilian, H. Mehrpouyan, Y. Hua, and H. Jafarkhani, "High-rate space coding for reconfigurable 2x2 millimeter-wave MIMO systems," 2015. [Online]. Available: <https://arxiv.org/abs/1505.06466>
- [27] M. R. Akdeniz, Y. Liu, M. K. Samimi, S. Sun, S. Rangan, T. S. Rappaport, and E. Erkip, "Millimeter wave channel modeling and cellular capacity evaluation," *IEEE J. Sel. Areas Commun.*, vol. 32, no. 6, pp. 1164–1179, June 2014.
- [28] A. M. Sayeed and V. Raghavan, "Maximizing MIMO capacity in sparse multipath with reconfigurable antenna arrays," *IEEE J. Sel. Signal Process.*, vol. 1, no. 1, pp. 156–166, June 2007.
- [29] A. M. Khalat, *Multifunctional reconfigurable antennas and arrays operating at 60 GHz band*. PhD thesis, UTAH STATE UNIVERSITY, 2017.
- [30] Y. Zhou, X. Chen, C. Ko, Z. Yang, C. Mouli, and S. Ramanathan, "Voltage-triggered ultrafast phase transition in vanadium dioxide switches," *IEEE Electron Device Lett.*, vol. 34, no. 2, pp. 220–222, Feb. 2013.
- [31] C. Waldschmidt and W. Wiesbeck, "Compact wide-band multimode antennas for MIMO and diversity," *IEEE Trans. Antennas Propag.*, vol. 52, no. 8, pp. 1963–1969, Aug. 2004.
- [32] G. H. Huff and J. T. Bernhard, "Integration of packaged RF MEMS switches with radiation pattern reconfigurable square spiral microstrip antennas," *IEEE Trans. Antennas Propag.*, vol. 54, no. 2, pp. 464–469, Feb. 2006.
- [33] H. Aissat, L. Cirio, M. Grzeskowiak, J. M. Laheurte, and O. Picon, "Reconfigurable circularly polarized antenna for short-range communication systems," *IEEE Trans. Microw. Theory Techn.*, vol. 54, no. 6, pp. 2856–2863, June 2006.
- [34] F. Sohrabi and W. Yu, "Hybrid analog and digital beamforming for mmwave OFDM large-scale antenna arrays," *IEEE J. Sel. Areas Commun.*, vol. 35, no. 7, pp. 1432–1443, July 2017.
- [35] C. Rusu, R. Mèndez-Rial, N. González-Prelcic, and R. W. Heath, "Low complexity hybrid precoding strategies for millimeter wave communication systems," *IEEE Trans. Wireless Commun.*, vol. 15, no. 12, pp. 8380–8393, Dec. 2016.
- [36] F. Sohrabi and W. Yu, "Hybrid digital and analog beamforming design for large-scale antenna arrays," *IEEE J. Sel. Signal Process.*, vol. 10, no. 3, pp. 501–513, Apr. 2016.
- [37] C. E. Chen, "An iterative hybrid transceiver design algorithm for millimeter wave MIMO systems," *IEEE Wireless Commun. Lett.*, vol. 4, no. 3, pp. 285–288, June 2015.
- [38] P. V. Amadori and C. Masouros, "Low RF-complexity millimeter-wave beamspace-MIMO systems by beam selection," *IEEE Trans. Commun.*, vol. 63, no. 6, pp. 2212–2223, June 2015.
- [39] C. Gustafson, K. Haneda, S. Wyne, and F. Tufvesson, "On mm-wave multipath clustering and channel modeling," *IEEE Trans. Antennas Propag.*, vol. 62, no. 3, pp. 1445–1455, Mar. 2014.
- [40] R. W. Heath, N. González-Prelcic, S. Rangan, W. Roh, and A. M. Sayeed, "An overview of signal processing techniques for millimeter wave MIMO systems," *IEEE J. Sel. Signal Process.*, vol. 10, no. 3, pp. 436–453, Apr. 2016.
- [41] A. M. Sayeed, "Deconstructing multiantenna fading channels," *IEEE Trans. Signal Process.*, vol. 50, no. 10, pp. 2563–2579, Oct. 2002.
- [42] D. Tse and P. Viswanath, *Fundamentals of Wireless Communication*. Cambridge University Press, 2005.
- [43] J. Brady, N. Behdad, and A. M. Sayeed, "Beamspace MIMO for millimeter-wave communications: System architecture, modeling, analysis, and measurements," *IEEE Trans. Antennas Propag.*, vol. 61, no. 7, pp. 3814–3827, July 2013.
- [44] V. Raghavan and A. M. Sayeed, "Sublinear capacity scaling laws for sparse MIMO channels," *IEEE Trans. Inf. Theory*, vol. 57, no. 1, pp. 345–364, Jan. 2011.
- [45] X. Gao, L. Dai, and A. M. Sayeed, "Low RF-complexity technologies to enable millimeter-wave MIMO with large antenna array for 5G wireless communications," *IEEE Commun. Mag.*, vol. 56, no. 4, pp. 211–217, Apr. 2018.
- [46] B. Wang, L. Dai, Z. Wang, N. Ge, and S. Zhou, "Spectrum and energy-efficient beamspace MIMO-NOMA for millimeter-wave communications using lens antenna array," *IEEE J. Sel. Areas Commun.*, vol. 35, no. 10, pp. 2370–2382, Oct. 2017.

- [47] J. Mo, P. Schniter, N. G. Prelicic, and R. W. Heath, "Channel estimation in millimeter wave MIMO systems with one-bit quantization," in *Proc. Asilomar Conf. Signals Syst. Comput.*, Nov. 2014, pp. 957–961.
- [48] V. Raghavan, A. S. Y. Poon, and V. V. Veeravalli, "MIMO systems with arbitrary antenna array architectures: Channel modeling, capacity and low-complexity signaling," in *Proc. Asilomar Conf. Signals Syst. Comput.*, Nov. 2007, pp. 1219–1223.
- [49] D. Huang, V. Raghavan, A. S. Y. Poon, and V. V. Veeravalli, "Angular domain processing for MIMO wireless systems with non-uniform antenna arrays," in *Proc. Asilomar Conf. Signals Syst. Comput.*, Oct. 2008, pp. 2043–2047.
- [50] A. Maltsev, V. Erceg, E. Perahia, C. Hansen, R. Maslennikov, A. Lomayev, A. Sevastyanov, A. Khoryaev, G. Morozov, M. Jacob, S. Priebe, T. Kürner, S. Kato, H. Sawada, K. Sato, and H. Harada, "Channel models for 60 GHz WLAN systems," *IEEE Document 802.11-09/0334r6*, Jan. 2010.
- [51] A. L. Moustakas, S. H. Simon, and A. M. Sengupta, "MIMO capacity through correlated channels in the presence of correlated interferers and noise: a (not so) large N analysis," *IEEE Trans. Inf. Theory*, vol. 49, no. 10, pp. 2545–2561, Oct. 2003.
- [52] C. Martin and B. Ottersten, "Asymptotic eigenvalue distributions and capacity for MIMO channels under correlated fading," *IEEE Trans. Wireless Commun.*, vol. 3, no. 4, pp. 1350–1359, July 2004.
- [53] V. Raghavan, A. Partyka, A. Sampath, S. Subramanian, O. H. Koymen, K. Ravid, J. Cezanne, K. Mukkavilli, and J. Li, "Millimeter-wave MIMO prototype: Measurements and experimental results," *IEEE Commun. Mag.*, vol. 56, no. 1, pp. 202–209, Jan. 2018.
- [54] V. Raghavan, A. Partyka, L. Akhondzadeh-Asl, M. A. Tassoudji, O. H. Koymen, and J. Sanelli, "Millimeter wave channel measurements and implications for phy layer design," *IEEE Trans. Antennas Propag.*, vol. 65, no. 12, pp. 6521–6533, Dec. 2017.
- [55] I. E. Telatar, "Capacity of multiantenna Gaussian channels," *Eur. Trans. Telecommun.*, vol. 10, no. 6, p. 586595, Nov./Dec. 1999.
- [56] P. Smith and M. Shafi, "An approximate capacity distribution for MIMO systems," *IEEE Trans. Commun.*, vol. 52, no. 6, pp. 887–890, June 2004.
- [57] S. Sanayei and A. Nosratinia, "Capacity maximizing algorithms for joint transmit-receive antenna selection," in *Proc. ACSSC*, vol. 2, Nov. 2004, pp. 1773–1776.
- [58] M. Gharavi-Alkhansari and A. B. Gershman, "Fast antenna subset selection in MIMO systems," *IEEE Trans. Signal Process.*, vol. 52, no. 2, pp. 339–347, Feb. 2004.
- [59] F. Khan and Z. Pi, "Millimeter-wave mobile broadband (MMB): Unleashing 3–300 GHz spectrum," in *Proc. IEEE Sarnoff Symp.*, May 2011, pp. 1–6.